Utilization of an Optimized AlphaFold Protein Model for Structure-Based Design of a Selective HDAC11 Inhibitor with Anti-neuroblastoma Activity

Fady Baselious[1], Sebastian Hilscher[1], Sven Hagemann[2], Sunita Tripathee[2], Dina Robaa[1], Cyril Barinka[3], Stefan Hüttelmaier[2], Mike Schutkowski[4], Wolfgang Sippl[1]*

1 Department of Medicinal Chemistry, Institute of Pharmacy, Martin-Luther-University of Halle-Wittenberg, 06120 Halle (Saale), Germany

2 Institute of Molecular Medicine, Martin Luther University Halle-Wittenberg, 06120 Halle (Saale), Germany

3 Institute of Biotechnology of the Czech Academy of Sciences, BIOCEV, 252 50 Vestec, Czech Republic

4 Charles Tanford Protein Center, Department of Enzymology, Institute of Biochemistry and Biotechnology, Martin-Luther-University of Halle-Wittenberg, 06120 Halle (Saale), Germany

*Corresponding author: Wolfgang Sippl

E-mail: wolfgang.sippl@pharmazie.uni-halle.de

Abstract:

AlphaFold is an artificial intelligence approach for predicting the 3D structures of proteins with atomic accuracy. One challenge that limits the use of AlphaFold models for drug discovery is the correct prediction of folding in the absence of ligands and cofactors, which compromises their direct use. We have previously described the optimization and use of the HDAC11-AlphaFold model for the docking of selective inhibitors such as FT895 and SIS17. Based on the predicted binding mode of FT895 in the optimized HDAC11 AlphaFold model, a new scaffold for HDAC11 inhibitors was designed, and the resulting compounds were tested in vitro against various HDAC isoforms. Compound **5a** proved to be the most active compound with an IC_{50} of 365 nM and was able to selectively inhibit HDAC11. **5a** also showed promising activity with an EC_{50} of 3.6 µM on neuroblastoma cells. Furthermore, we supported our study by comparative docking and MD simulations.

Keywords:

AlphaFold; HDAC11; Structure based drug design; Model optimization; In vitro assay; Neuroblastoma; Docking; Molecular dynamics simulation

1 Introduction:

Histone deacetylases (HDACs) are enzymes that catalyze the removal of the acetyl group from the lysine residue of histone protein leading to condensed chromatin structures, a process that suppresses transcription [1]. The histone deacetylase family is classified into four classes. Eleven zinc dependent HDACs have been identified so far and constitute class I, class II and class IV of the family with HDAC11 being the only member of class IV [2]. There is growing evidence that HDAC11 is implicated in various pathophysiological processes [3, 4] including various carcinomas [4-8]. These findings establish HDAC11 as a potential target for anti-cancer therapeutics.

Few selective HDAC11 inhibitors have been reported in literature. FT895 is a hydroxamic acid based HDAC11 selective inhibitor that was reported by Forma Therapeutics [9] and could significantly reduce non-small cell lung cancer cells viability [10]. Recently, Bai et al. reported the development of PB94, which also bears a hydroxamic acid moiety as zinc binding group and demonstrated beneficial effect in a neuropathic pain mouse model [11]. Since the defatty-acylase activity of HDAC11 is confirmed [12, 13], the ability of HDAC11 to accommodate longer alkyl chain was exploited for the design and development of selective inhibitors as the alkyl hydrazide derivative SIS17 which bears a 16 carbon long alkyl chain [14] and the natural product trapoxin A analogue TD034 [15].

Currently, there is no crystal structure reported for HDAC11. The low sequence identity of HDAC11 catalytic domain with other HDAC family members [16, 17] affects the reliability of the conventional template based homology modeling. AlphaFold models, which are produced by a neural network artificial intelligence (AI) approach demonstrate highly accurate predictions of the 3D protein structures even in absence of known similar structures [18, 19]. Two studies reported the successful utilization of AlphaFold models using AI molecular generation methods to design novel inhibitors for cyclin dependent kinase 20 (CDK20) and salt inducible kinase 2 (SIK2) [20, 21].

However, AlphaFold models demonstrated worse performance in several studies when assessed for docking or virtual screening in comparison to their corresponding crystal structures [22-26] which suggests that further refinement is required for AlphaFold models prior to utilization for the aim of drug design and discovery.

We previously optimized the HDAC11 AlphaFold model [16] by docking the zinc ion into the protein model followed by minimization in presence of HDAC11 inhibitors which were also found co-crystallized with HDAC8. Moreover, we showed that the optimized model could be successfully used for docking of HDAC11 selective inhibitors as FT895 and SIS17. In the current study we further employed the predicted binding mode of HDAC11 inhibitors in the AlphaFold model for the rational structure based

design of selective inhibitors with novel scaffolds. The developed compounds were assessed by in vitro testing and the most active and selective compound was evaluated for its anti-neuroblastoma activity in cancer cells. Additionally we conducted a comparative docking study as well as molecular dynamics simulations to investigate the binding mode and rationalize the detected activity and selectivity.

2 Material and Methods:

2.1 Computational modeling:

The computational modeling was performed using Schrödinger Suite 2019 and Maestro [27] for visualization.

2.1.1 Protein preparation:

Protein structures were prepared using the Protein Preparation Wizard [28, 29] by adding hydrogen atoms and assigning bond orders. Zero order bonds to metals were generated and water molecules (when available in the X-ray structure) 5 Å away from the ligands were removed. Ionization states of the ligands were generated using Epik [30-32] at pH 7.0 ±2.0. The hydroxamate [16, 33-36] form of the ligands was selected for further hydrogen bond optimization. Hydrogen bond optimization was assigned specifying the protonated state of His142 (HDAC11 numbering) in the HIP form with sampling water orientation and using PROPKA at pH 7.0.

2.1.2 Ligand preparation:

The designed compounds and the co-crystallized ligands were prepared using LigPrep [37] panel with OPLS3e [38-41] force fields. The compounds were prepared in the deprotonated hydroxamate form.

2.1.3 Docking:

The binding mode of the most active and selective compound **5a** was studied by docking. Receptor grids were generated using the Receptor Grid Generation panel utilizing the centroid of the co-crystallized ligands. All grids were generated with the protonated His142 in HIP state. Docking was performed using Glide [42-45] with specifying standard precision mode and flexible ligand sampling utilizing OPLS3e force field. For HDAC11, docking was performed in the grid obtained from TSA-HDAC11 AlphaFold model complex with flipped-out Phe152 [16]. For the other HDAC isoforms the following crystal structures were used: HDAC1 (PDB 5ICN), HDAC6 (PDB 5EDU) and HDAC8 (PDB 5FCW).

Re-docking of the co-crystallized ligands was performed in order to validate the docking protocol. The RMSD for the docked and the native poses was found to be 2.018 Å, 0.763 Å and 0.369 Å for HDAC1, HDAC6 and HDAC8, respectively.

2.1.4 Molecular dynamics simulation:

The initially predicted binding mode of **5a** was further studied by molecular dynamics simulations using Desmond software [46, 47]. The system was solvated in SPC water model using an orthorhombic box and a buffer distance of 10 Å. The box volume was then minimized and neutralization of the system was performed by addition of chloride ions 4 Å away from the ligand.

The solvated system was relaxed using the default Desmond relaxation protocol for NPT ensemble followed by a production run utilizing the NPT ensemble at pressure of 1.01325 bar using Martyna-Tobias-Klein barostat and temperature of 300 K using a Nose–Hoover chain thermostat.

Analysis of the RMSD values and distances was performed using the Simulation Event Analysis panel. The RMSD values of the protein were calculated using the backbone atoms while the ligand and zinc ion RMSD values were calculated after fitting to the protein backbone. The Simulation Interaction Diagram panel was used for analyzing the RMSF and the interaction persistence of the ligands. RMSD and RMSF values of the protein were calculated excluding the termini (residues: 1-14 and 321-347, HDAC11 numbering).

2.2 Chemistry:

2.2.1 General

Materials and reagents were purchased from Sigma-Aldrich Co. Ltd (St. Louis, MI, USA) and abcr GmbH (Karlsruhe, Germany). Analytically pure and dry solvents were used. Thin layer chromatography was performed on aluminum sheets coated with silica gel 60 F254 (Merck, Darmstadt, Germany). For medium pressure chromatography (MPLC), silica gel Biotage® (Biotage, Uppsala, Sweden) SNAP ultra-HP-sphere 25 µm containing columns were used.

The purity of the final compounds were determined using high-pressure liquid chromatography (HPLC). Purity was measured by UV absorbance at 254 nm. The HPLC system employed two LC-10AD pumps, a SPD-M10A VP PDA detector, and a SIL-HT autosampler, all from the manufacturer Shimadzu (Kyoto, Japan). Merck LiChrospher 100 RP18, 125 mm x 4 mm, 5 µm column was used. Mobile phase composition was Methanol, H_2O, and 0.05% trifluroacetic acid.

High-resolution mass spectrometry (HRMS-ESI) analyses was performed with a LTQ(linear ion trap) Orbitrap XL hybrid mass spectrometer (Thermo FisherScientific). ^{1}HNMR and ^{13}CNMR spectra were taken on a Varian Inova 400using using deuterated dimethyl sulfoxide (DMSO-d6) as solvent. Chemical shifts were referenced to the residual solvent signals

2.2.2 General procedures for synthesis of chalcones (2a-b):

A mixture of equimolar amounts (25 mmol) of 2-methylacetophenone **1** and the appropriate aromatic aldehyde in absolute ethanol (25 ml) containing NaOH (25 mmol), was stirred at room temperature overnight. In the case of benzaldehyde, the reaction mixture was diluted with water and extracted with ethyl acetate. The organic layer was dried over anhydrous sodium sulfate, filtered, and evaporated under vacuum to afford yellow oil as product **2a**. In the case of 3,4-dichlorobenzaldehyde the solid precipitate was filtered, and washed with methanol to afford yellow powder as product **2b**.

2.2.2.1. ***(2E)-1-(2-methylphenyl)-3-phenylprop-2-en-1-one (2a).*** Yellow oil, ^{1}H NMR (400 MHz, DMSO-d_6) δ 7.78 – 7.71 (m, 2H), 7.62 – 7.57 (m, 1H), 7.51 – 7.35 (m, 6H), 7.34 – 7.28 (m, 2H), 2.35 (s, 3H). Yield, 67.87%.

2.2.2.2. ***(2E)-3-(3,4-dichlorophenyl)-1-(2-methylphenyl)prop-2-en-1-one (2b)*** Yellow powder, ^{1}H NMR (400 MHz, DMSO-d_6) δ 8.13 (d, *J* = 2.0 Hz, 1H), 7.80 – 7.73 (m, 1H), 7.71 – 7.61 (m, 2H), 7.57 – 7.39 (m, 3H), 7.36 – 7.26 (m, 2H), 2.37 (s, 3H). Yield, 72.16%.

2.2.3 General procedures for the synthesis of pyrazol-3-yl-benzoic acids (3a-b):

A mixture of equimolar amounts (3.5 mmol) of the appropriate chalcone **2a-b** and substituted hydrazine in absolute ethanol was stirred overnight in the presence of catalytic amounts (100 mg) of thiamine HCL. The reaction mixture was diluted with water and extracted with ethyl acetate. The organic layer was dried over anhydrous sodium sulfate, filtered, and evaporated under reduced pressure to afford orange yellow oil as product.

The obtained crude product, without further purification, was dissolved in a mixture of water and pyridine (50:50). The mixture was heated under reflux and excess of potassium permanganate (18 mmol) was added portion wise. Heating under reflux was continued for 48 hours. The reaction mixture was then cooled and filtered. The filtrate was neutralized with concentrated HCl affording the product as solid precipitate. The obtained precipitate was then filtered and dried. For purification, the obtained solid was dissolved in a warm aqueous solution of sodium hydroxide. The solution was filtered and re-acidified by aqueous HCl. The obtained solid was then filtered and dried to afford the products **3a-b**.

2.2.3.1. ***2-(1,5-diphenyl-1H-pyrazol-3-yl)benzoic acid (3a).*** White solid, ^{1}H NMR (400 MHz, DMSO-d_6) δ 12.86 (s, 1H), 7.76 (dd, *J* = 7.8, 1.2 Hz, 1H), 7.61 – 7.52 (m, 2H), 7.48 – 7.33 (m, 7H), 7.32 – 7.21 (m, 4H), 6.87 (s, 1H). Yield, 51.2%.

2.2.3.2. ***2-(1-methyl-5-phenyl-1H-pyrazol-3-yl)benzoic acid (3b).*** White solid, ^{1}H NMR (400 MHz, DMSO-d_6) δ 12.84 (s, 1H), 7.70 – 7.65 (m, 1H), 7.57 – 7.47 (m, 6H), 7.46 – 7.42 (m, 1H), 7.40 – 7.37 (m, 1H), 6.57 (s, 1H), 3.86 (s, 3H). Yield, 60.57%.

2.2.3.3. ***2-[5-(3,4-dichlorophenyl)-1-phenyl-1H-pyrazol-3-yl]benzoic acid (3c).*** Yellow solid, ^{1}H NMR (400 MHz, DMSO-d_6) δ 12.86 (s, 1H), 7.73 (dd, *J* = 7.8, 1.3 Hz, 1H), 7.65 – 7.50 (m, 4H), 7.49 – 7.36 (m, 4H), 7.35 – 7.29 (m, 2H), 7.14 (dd, *J* = 8.4, 2.1 Hz, 1H), 7.00 (s, 1H). Yield, 61.08%.

2.2.3.4. ***2-[5-(3,4-dichlorophenyl)-1-methyl-1H-pyrazol-3-yl]benzoic acid (3d).*** White solid, ^{1}H NMR (400 MHz, DMSO-d_6) δ 12.83 (s, 1H), 7.86 (d, *J* = 2.1 Hz, 1H), 7.76 (d, *J* = 8.4 Hz, 1H), 7.65 (dd, *J* = 7.8, 1.3 Hz, 1H), 7.59 – 7.47 (m, 3H), 7.43 – 7.35 (m, 1H), 6.68 (s, 1H), 3.89 (s, 3H). Yield, 52.67%.

2.2.4 General procedures for amide coupling (4a-b):

A mixture of the obtained acid **3a-b** (1.3 mmol) and hexafluorophosphate azabenzotriazole tetramethyl uronium (HATU) (1.3 mmol) in DMF was stirred for 15 min after which O-(tetrahydro-2*H*-pyran-2-yl)-hydroxylamine (1.4 mmol) and N,N-diisopropylethylamine (DIPEA) (3.9 mmol) were added and stirring was continued for 3-4 hours. The reaction mixture was diluted with water and extracted with ethyl acetate. The organic layer was washed with saturated solutions of ammonium chloride and sodium carbonate followed by brine. The organic layer was dried over anhydrous sodium sulfate and evaporated under reduced pressure. The product was purified by medium pressure liquid chromatography (MPLC) using a gradient of ethyl acetate/n-heptane.

2.2.4.1. ***2-(1,5-diphenyl-1H-pyrazol-3-yl)-N-(oxan-2-yloxy)benzamides (4a).*** White solid, ^{1}H NMR (400 MHz, DMSO-d_6) δ 11.48 (s, 1H), 7.93 – 7.86 (m, 1H), 7.56 – 7.48 (m, 1H), 7.45 – 7.28 (m, 10H), 7.27 – 7.20 (m, 2H), 6.92 (s, 1H), 5.03 (t, *J* = 3.0 Hz, 1H), 3.98 – 3.88 (m, 1H), 3.37 – 3.31 (m, 1H), 1.72 – 1.59 (m, 3H), 1.53 – 1.41 (m, 3H). Yield 81.5%.

2.2.4.2. ***2-(1-methyl-5-phenyl-1H-pyrazol-3-yl)-N-(oxan-2-yloxy)benzamides (4b).*** White solid, ^{1}H NMR (400 MHz, DMSO-d_6) δ 11.43 (s, 1H), 7.80 (dd, *J* = 7.9, 1.2 Hz, 1H), 7.54 – 7.43 (m, 6H), 7.38 – 7.33 (m, 1H), 7.32 – 7.28 (m, 1H), 6.66 (s, 1H), 5.06 (t, *J* = 2.8 Hz, 1H), 3.98 – 3.90 (m, 1H), 3.87 (s, 3H), 3.42 – 3.35 (m, 1H), 1.73 – 1.62 (m, 3H), 1.53 – 1.43 (m, 3H). Yield 71.6%.

2.2.4.3. ***2-[5-(3,4-dichlorophenyl)-1-phenyl-1H-pyrazol-3-yl]-N-(oxan-2-yloxy)benzamides (4c).*** White solid, ^{1}H NMR (400 MHz, DMSO-d_6) δ 11.49 (s, 1H), 7.87 (dd, *J* = 7.8, 1.2 Hz, 1H), 7.61 (d, *J* = 8.4 Hz, 1H), 7.56 (d, *J* = 2.1 Hz, 2H), 7.48 – 7.31 (m, 7H), 7.09 (dd, *J* = 8.4, 2.1 Hz, 1H), 7.04 (s, 1H), 5.06 (t, *J* = 2.8 Hz, 1H), 4.01 – 3.92 (m, 1H), 3.42 – 3.32 (m, 1H), 1.73 – 1.60 (m, 3H), 1.55 – 1.43 (m, 3H). Yield 77.2%.

2.2.4.4. ***2-[5-(3,4-dichlorophenyl)-1-methyl-1H-pyrazol-3-yl]-N-(oxan-2-yloxy)benzamides (4d).*** White solid, ^{1}H NMR (400 MHz, DMSO-d_6) δ 11.46 (s, 1H), 7.83 (d, *J* = 2.1 Hz, 1H), 7.80 – 7.74 (m, 2H), 7.55 (dd, *J* = 8.4, 2.1 Hz, 1H), 7.51 – 7.44 (m, 1H), 7.40 – 7.34 (m, 1H), 7.33 – 7.28 (m, 1H), 6.76 (s, 1H),

5.10 (t, *J* = 2.5 Hz, 1H), 4.03 – 3.93 (m, 1H), 3.90 (s, 3H), 3.46 – 3.37 (m, 1H), 1.75 – 1.66 (m, 3H), 1.55 – 1.47 (m, 3H). Yield 70.7%.

2.2.5 General procedures for THP de-protection (5a-b):

The respective THP-protected hydroxamic acid **4a-b** (0.8 mmol) was dissolved in 20 mL of tetrahydrofuran, and 1 mL of 2N aqueous HCl was added, and the mixture was stirred overnight. The reaction mixture was diluted with water and extracted with ethyl acetate. The organic layer was dried over anhydrous sodium sulfate and evaporated under reduced pressure. The product was purified by medium pressure liquid chromatography (MPLC) using a gradient elution with methanol and dichloromethane.

2.2.5.1. ***2-(1,5-diphenyl-1H-pyrazol-3-yl)-N-hydroxybenzamide (5a).*** White solid, ^{1}H NMR (400 MHz, DMSO-d_6) δ 10.91 (s, 1H), 9.12 (s, 1H), 7.92 (dd, *J* = 7.8, 1.3 Hz, 1H), 7.52 – 7.46 (m, 1H), 7.44 – 7.30 (m, 10H), 7.26 – 7.22 (m, 2H), 6.84 (s, 1H). ^{13}C NMR (101 MHz, DMSO-d_6) δ 166.73, 149.98, 143.76, 140.03, 134.43, 131.04, 130.35, 129.88, 129.50, 129.07, 128.98, 128.94, 128.72, 128.43, 128.14, 125.48, 107.88. HRMS m/z: $[M + H]^+$ 356.1399; calculated $C_{22}H_{18}O_2N_3$: 356.1399. HPLC: rt 12.966 min (purity 99.60%). Yield 10.6%.

2.2.5.2. ***N-hydroxy-2-(1-methyl-5-phenyl-1H-pyrazol-3-yl)benzamides (5b).*** White solid, ^{1}H NMR (400 MHz, DMSO-d_6) δ 10.82 (s, 1H), 9.04 (s, 1H), 7.84 (dd, *J* = 7.9, 1.3 Hz, 1H), 7.57 – 7.41 (m, 6H), 7.36 – 7.30 (m, 1H), 7.29 – 7.25 (m, 1H), 6.59 (s, 1H), 3.88 (s, 3H). ^{13}C NMR (101 MHz, DMSO-d_6) δ 166.80, 147.85, 144.20, 134.14, 131.55, 130.41, 129.73, 129.26, 128.96, 128.90, 128.57, 128.11, 127.58, 105.73, 38.11. HRMS m/z: $[M + H]^+$ 294.1237; calculated $C_{17}H_{16}O_2N_3$: 294.1243. HPLC: rt 11.091 min (purity 96.93%). Yield 38.6%.

2.2.5.3. ***2-[5-(3,4-dichlorophenyl)-1-phenyl-1H-pyrazol-3-yl]-N-hydroxybenzamide (5c).*** White solid, ^{1}H NMR (400 MHz, DMSO-d_6) δ 10.91 (s, 1H), 9.11 (s, 1H), 7.90 (dd, *J* = 7.8, 1.3 Hz, 1H), 7.62 (d, *J* = 8.4 Hz, 1H), 7.55 (d, *J* = 2.1 Hz, 1H), 7.52 – 7.32 (m, 8H), 7.13 (dd, *J* = 8.4, 2.1 Hz, 1H), 6.92 (s, 1H). ^{13}C NMR (101 MHz, DMSO-d_6) δ 166.62, 150.16, 141.22, 139.57, 134.46, 131.85, 131.67, 131.23, 130.80, 130.79, 130.59, 129.93, 129.72, 129.06, 128.72, 128.54, 128.45, 128.31, 125.66, 108.47. HRMS m/z: [M + H] 424.0613; calculated $C_{22}H_{16}O_2N_3Cl_2$: 424.0620. HPLC: rt 14.541 min (purity 99.33%). Yield 12.6%.

2.2.5.4. ***2-[5-(3,4-dichlorophenyl)-1-methyl-1H-pyrazol-3-yl]-N-hydroxybenzamide (5d).*** White solid, ^{1}H NMR (400 MHz, DMSO-d_6) δ 10.83 (s, 1H), 9.06 (s, 1H), 7.85 – 7.80 (m, 2H), 7.77 (d, *J* = 8.3 Hz, 1H), 7.56 (dd, *J* = 8.3, 2.1 Hz, 1H), 7.49 – 7.42 (m, 1H), 7.38 – 7.32 (m, 1H), 7.30 – 7.26 (m, 1H), 6.66 (s, 1H), 3.90 (s, 3H). ^{13}C NMR (101 MHz, DMSO-d_6) δ 166.67, 148.00, 141.75, 134.17, 132.07, 131.77, 131.42, 131.30, 130.92, 130.57, 129.78, 129.09, 128.56, 128.15, 127.74, 106.34, 38.27. HRMS m/z: $[M + H]^+$ 362.0460; calculated $C_{17}H_{14}O_2N_3Cl_2$: 362.0463. HPLC: rt 13.398 min (purity 96.741%). Yield 37.0%.

2.3 In vitro enzymatic assay:

Human HDAC11 full-length protein was expressed and purified as described in previous work [13] . A fluorescence based HDAC11 enzymatic assay was used. The fluorescence measurements were performed using a PerkinElmer Envision 2104 multilabel plate reader (Waltham, MA, USA) at λ_{ex} = 320 nm and λ_{em} = 430 nm. The reaction mixture consisted of HDAC11, and the acylated peptide substrate derived from TNFα in a reaction buffer comprising 50 mM HEPES, 2 mg/mL BSA, and 70 μMTCEP, and at pH 7.4 which was adjusted with NaOH (total volume 40 μL). The reactions were incubated in black 384-well plates for 30 min (scan every 30 s) at room temperature, and the increase of relative fluorescence reflecting the product formation was monitored. As reference for HDAC11 inhibitors we used the reported compound SIS17 (purchased from MedChemExpress LLC, 1 Deer Park Dr, Suite Q, Monmouth Junction, NJ 08852, USA).

For HDAC1, 2, 3, 6 and HDAC6 the recombinant proteins were purchased from ENZO Life Sciences AG (Lausen, CH) whereas HDAC4, 5, 7, 9 and 10 were produced as described in previous work [48]. Human HDAC8 was produced as described in previous work [49]. All inhibitors were tested in an enzymatic in vitro assay as described before using 384-well plates (GreinerONe, catalogue no. 784900) [49]. After 5 minutes of incubation of the inhibitors with the respective enzymes (HDAC1 = 10 nM, HDAC2 and 3 = 3 nM, HDAC4 = 5 nM, HDAC5 = 10 nM, HDAC6 = 1 nM, HDAC7 = 5 nM, HDAC8 = 2 HDAC 9 = 20 nM, HDAC10 = 5 nM), the reactions were always started by the addition of substrate.

For HDAC1, 2, 3 and 6, an acetylated peptide substrate derived from p53 (Ac-RHKK(Acetyl)-AMC) was used in a discontinuous fluorescence assay as described before [48]. All reactions were performed in assay buffer (20 mM HEPES, 140 mM NaCl, 10 mM MgCl2, 1 mM TCEP and 0.2 mg/mL BSA, pH 7.4 adjusted with NaOH) at 37 °C. After 1 hour the reaction was quenched by adding trypsin and SAHA. The fluorescence intensity was measured after 1 hour of incubation using an Envision 2104 Multilabel Plate Reader (PerkinElmer, Waltham, MA), with an excitation wavelength of 380 ± 8 nm and an emission wavelength of 430 ± 8 nm.

HDAC4, 5, 7, 8, 9 and 10 were measured in a continuous manner using the thio-acetylated peptide substrate (Abz-SRGGK(thio-TFA)FFRR-NH2), which was described before [48]. For HDAC 10, an internal quenched spermidine-like substrate was used.

The fluorescence increase was followed for 1 hour with two reads per min with an excitation wavelength of 320 ± 8 nm and an emission wavelength of 430 ± 8 nm. Positive (enzyme, substrate, DMSO and buffer) and negative (substrate, DMSO and Buffer) controls were included in every measurement and

were set as 100 and 0 %, respectively and the measured values were normalized accordingly. All tests were done in three replicates.

2.4 Anti-neuroblastoma evaluation:

To ascertain the EC50 values of SIS17 and compound 5a in neuroblastoma, BE(2) C cells were seeded in a 96-well plate. Subsequently, a progressive dilution series of the compounds was executed, and these compounds were added to the cells alongside dimethyl sulfoxide (DMSO) as a control condition. Following a 72 h treatment duration, the cell viability was quantified and adjusted relative to the DMSO control. The determination of EC_{50} values was achieved through the utilization of GraphPad Prism software (version 10.1.1) employing non-linear regression analysis. The tests were carried out in four replicates.

3 Results and discussion:

3.1 Structure Based Design:

As shown in our previous study, the predicted binding mode of the selective inhibitor FT895 in the refined HDAC11 AlphaFold model demonstrated the typical interactions for hydroxamic acids showing a bidentate chelation of the zinc ion through the two oxygen atoms of the hydroxamate moiety along with the salt bridge and two hydrogen bond interactions with His142, His143 and Tyr304, respectively. Additionally, the ligand was sandwiched between the side chains of Tyr209 and Leu268 of loop 5 and loop 6, respectively with which it formed hydrophobic interactions (**Figure 1A**).

To further examine the significance of the predicted binding mode of FT895 and the applicability of the optimized model, we aimed to develop probes bearing new scaffolds based on the observed docked pose of FT895, In the newly designed compounds the linear shape of the ligand along with the ortho substitution pattern to the hydroxamic acid moiety were kept, since these were considered as selectivity determinant for HDAC11. As the structure of FT895 is accommodated between the side chains of residues Tyr209 and Leu268 of loop 5 and loop 6 respectively, we thought of designing branched ligands (**Figure 1B**) by extending various groups that are directed towards loop 1, thus making interactions with loop 1 residues and blocking the binding site from both sides with the aim of maintaining selectivity and increasing activity. The new scaffold was designed to be synthetically accessible through Claisen Schmidt condensation followed by cyclization using substituted hydrazines, a pathway that would allow for the chemical modification of the branching substructures and their substitutions easily.

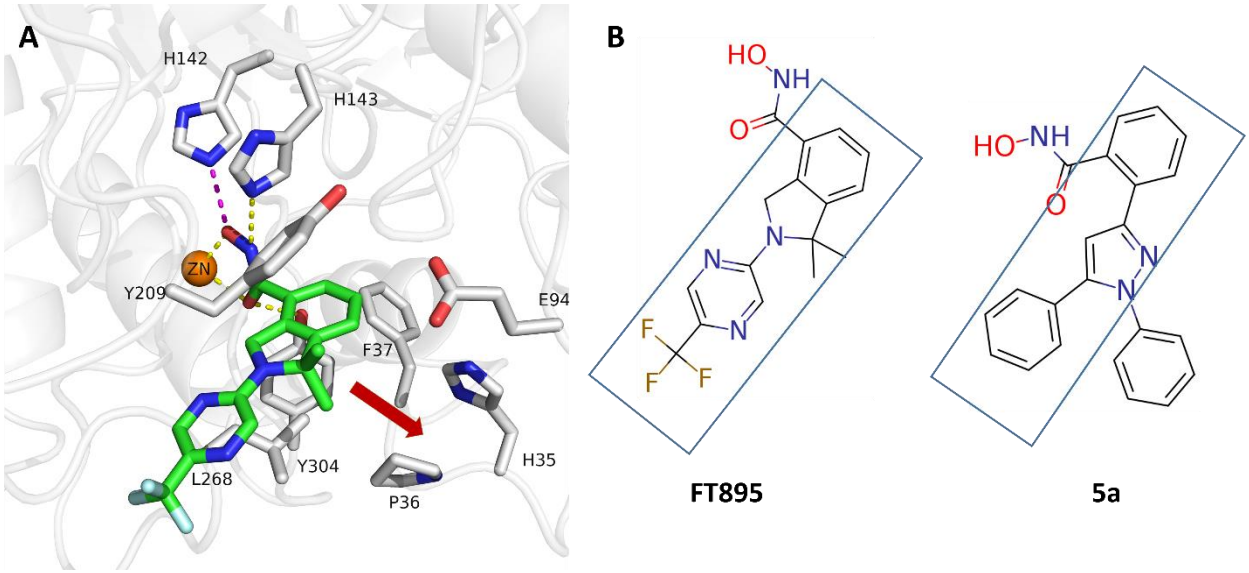

Figure 1. Representation of the structure-based design strategy applied in the current study. (**A)** Docking pose of the selective ligand FT895 in the optimized HDAC11 AlphaFold model. The protein backbone appears as white cartoon, residues as grey sticks, zinc cofactor as orange sphere and FT895 as green sticks. Hydrogen bonds and coordination bonds are represented as yellow dashed lines and the salt bridge as magenta dashed lines. The red arrow points towards loop1, highlighting the position for additional structure feature. (**B)** Schematic diagram representing the design of compound **5a** based on the ligand FT895, highlighting the similarities in linear structure along with ortho substitution and additional structural features in **5a** directed towards loop 1.

3.2 Chemistry:

Starting from the commercially available 2-methylacetophenone **1** and by reaction with aromatic aldehydes in the presence of alcoholic NaOH, the corresponding chalcones **2a-b** were obtained. The chalcones were further cyclized using substituted hydrazines in the presence of thiamine hydrochloride as catalyst [50]. The reaction afforded a mixture of pyrazole/pyrazoline products. The crude product from the cyclization reaction was used without further purification for the oxidation reaction by heating under reflux with potassium permanganate in mixture of water and pyridine to afford the corresponding carboxylic acid pyrazole derivatives **3a-d**. The obtained acid was then coupled with *O*-(tetrahydro-2*H*-pyran-2-yl)-hydroxylamine in the presence of HATU and using DIPEA as base to afford the corresponding THP-protected derivatives **4a-d**, which were subsequently deprotected using aqueous HCl in THF to afford the final hydroxamic acid products **5a-d**.

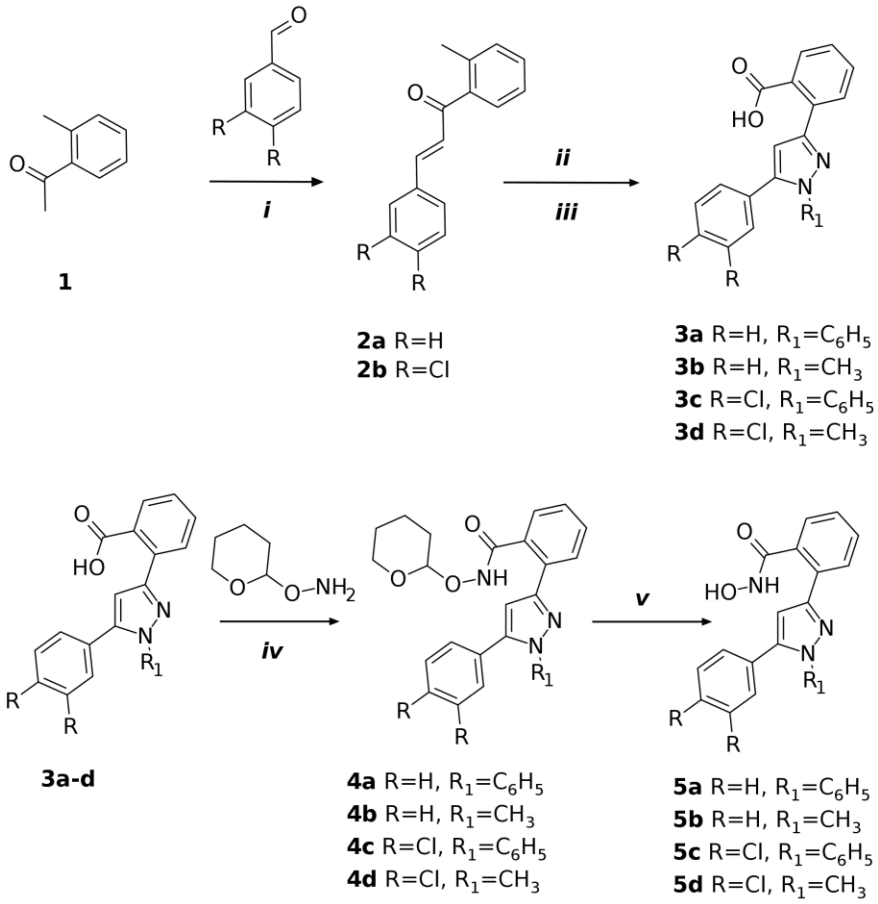

Scheme 1: Synthesis of target compounds. **Reagents and conditions:** (*i*) Alcoholic NaOH/RT/ overnight; (*ii*) NH_2NHR_1/Thiamine.HCl/ethanol/RT/overnight; (*iii*) $KMnO_4/H_2O$:pyridine (50:50)/reflux/48 h; (*iv*) DMF/HATU/DIPEA/RT/3-4 h; (*v*) THF/aq. HCl/RT/overnight.

3.3 In vitro Enzymatic Evaluation and Anti-Neuroblastoma Activity:

The four synthesized compounds were first screened for their enzymatic inhibitory activity at 10 µM concentration against the main target, HDAC11. The screening was also performed for HDAC1, HDAC6 and HDAC8 as representative candidates from class1 and class II HDACs. For HDAC1 and HDAC6 no inhibition could be observed for all compounds. For HDAC11, the compounds demonstrated inhibition percent ranging between 79% and 98%. For HDAC8 weak inhibition between 30% and 65% was observed (**Figure 2A**). Profiling the IC_{50} values of the four compounds for HDAC11 showed that the most active compound is **5a** demonstrating an IC_{50} value of 365±16 nM, while the IC_{50} values of the other three compounds are in the micromolar range between 3 and 4 µM (**Figure 2B, Table 1**). Interestingly the most active compound **5a** is also the most selective one showing only around 30% inhibition of HDAC8. Furthermore, we screened compound **5a** against all other isoforms of HDACs and no or very weak inhibition could be observed (**Figure 3)**. When comparing the IC_{50} with the previously reported HDAC11 inhibitor FT895, it is important to consider the variation in IC_{50} when using different substrates

for the evaluation of the inhibitory activity. FT895 showed an HDAC11 IC_{50} value of 0.003 µM [9] when using a non-native triflouroacetyl lysine substrate and an IC_{50} value of 0.74 µM [14] when using a myristoyl-H3K9 peptide which is more similar to the physiologic substrate. The HDAC11 in vitro assay used in the current work also utilized a myristoylated peptide [12]. As reference we included the reported HDAC11 selective inhibitor SIS17 in our assay and measured an IC_{50} value of 0.17 µM. Thus our results show that **5a** has a similar in vitro activity compared to FT895 and SIS17 and retained promising selectivity.

Since the depletion of HDAC11 in MYCN-driven neuroblastoma cells was reported to induce cell death through caspase mediated apoptosis [51] we further evaluated compound **5a** for its anti-neuroblastoma activity using the BE(2)-C neuroblastoma cell line. Interestingly the compound showed promising activity as it could inhibit the viability of the neuroblastoma cells with EC_{50} value of about 3.6 µM. We also tested the reported inhibitor SIS17 for its effect in the BE(2)-C neuroblastoma cell line and measured a weaker inhibition (EC_{50} > 10.0 µM).

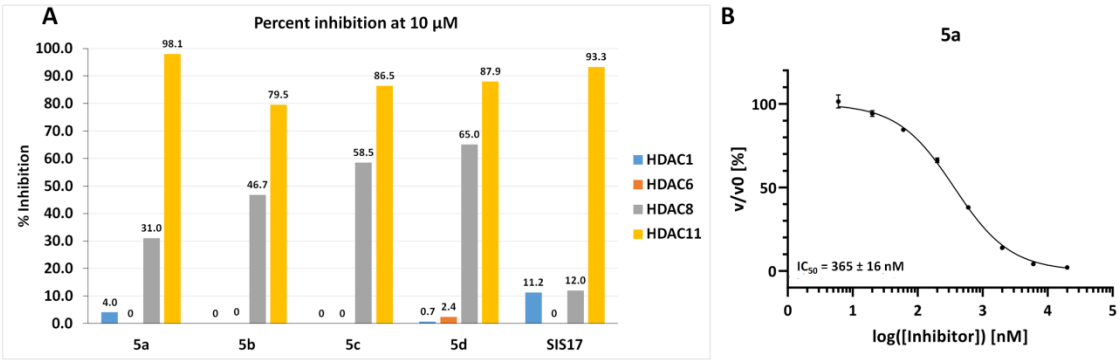

Figure 2. (**A**) Percentage inhibition of HDAC1, HDAC6, HDA8 and HDAC11 enzyme activity at 10 µM inhibitor concentration. (**B**) IC_{50} curve of the best candidate **5a** for HDAC11.

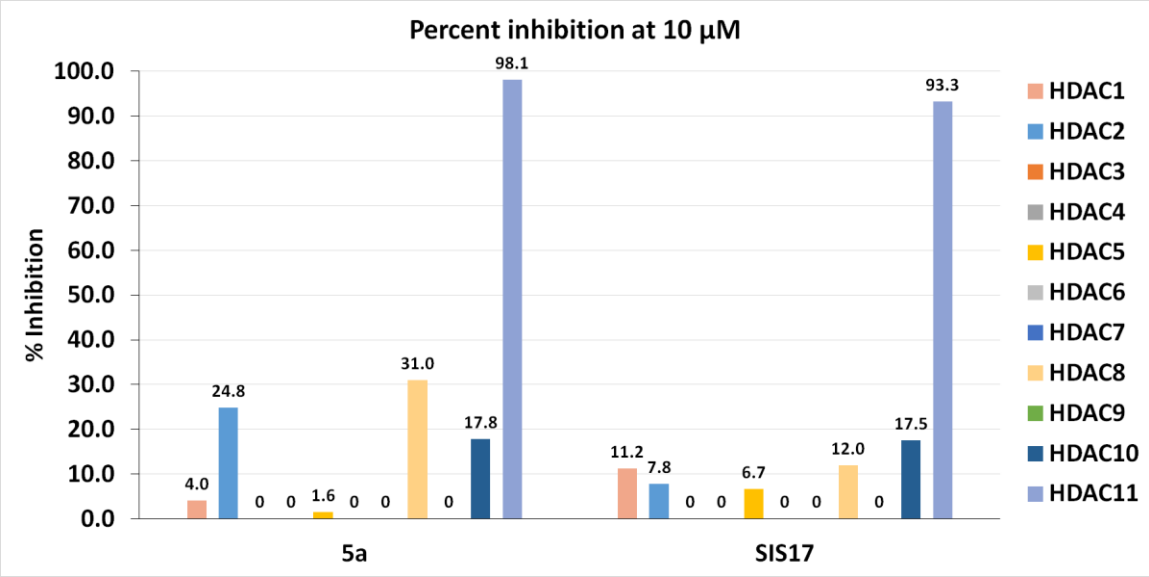

Figure 3. Percent enzymatic activity at 10 µM concentration for SIS17 and compound **5a** for all HDAC subtypes.

Table 1: IC_{50} values of the synthesized inhibitors in nM for HDAC11.

IC_{50} HDAC11		
Compound	**nM**	**SD**
5a	365	16
5b	4000	517
5c	3100	491
5d	3900	593
SIS17	170	20

3.4 Docking:

Comparing the docking poses of **5a** and FT895 (**Figure 4**) shows that the benzohydroxamate moiety of **5a** is inserted deeper in the binding pocket allowing for one terminal phenyl ring to be sandwiched between the side chains of Tyr209 and Leu268 with which it forms hydrophobic interactions, while the other phenyl ring attached to the pyrazole nitrogen is directed towards loop 1 and forming hydrophobic interactions with Pro36 thus fulfilling the aim of the design.

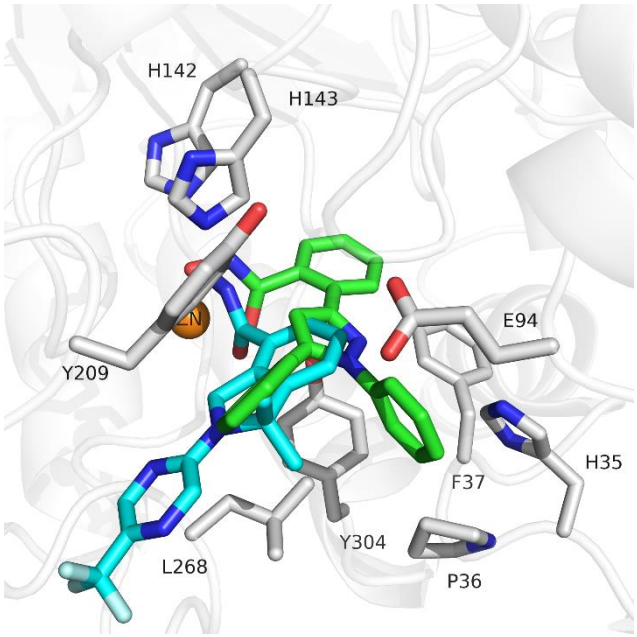

Figure 4. Superposition of the docked poses of FT895 and **5a** in HDAC11 highlighting the difference in the orientation of the benzohydroxamate and the position of the terminal phenyl ring extension. The protein backbone appears as white cartoon, residues as grey sticks, zinc cofactor as orange sphere **5a** as green sticks and FT895 as cyan sticks.

Docking of the most active and selective compound **5a** was performed in the refined HDAC11 AlphaFold model as well as HDAC1, HDAC6 and HDAC8. For the optimized HDAC11 AlphaFold model the docking was performed in the complex minimized in presence of TSA and using the grid with flipped-out Phe152 as it showed the best docking results in our pervious study [16]. The obtained pose of **5a** in HDAC11, demonstrated bidentate chelation of the zinc ion through the two oxygen atoms of the hydroxamate zinc binding group with distances of 2.18 Å and 2.17 Å for the hydroxyl oxygen and the carbonyl oxygen, respectively. A salt bridge is formed between the deprotonated oxygen of the hydroxamate and His142. Furthermore, a hydrogen bond interaction is observed between the carbonyl oxygen of the hydroxamate moiety and Tyr304. Additionally, the ligand formed two π-π interactions through the pyrazole ring and one terminal phenyl ring with Tyr304 and Tyr209, respectively (**Figure 5A**).

Docking of **5a** in HDAC1 and HDAC6 (**Figures 5B** and **5C**) demonstrated that the ligand could not be placed into the binding site and failed to show effective chelation of the zinc ion. The obtained pose of **5a** in HDAC8 showed an orientation in which the ligand was not able to chelate the zinc ion in the correct bidentate fashion or show the interactions commonly observed for HDAC8 co-crystallized hydroxamic acid inhibitors (**Figure 5D**). Interestingly the results from the docking study are in agreement with the results from the in vitro activity evaluation which further reflects the success of adopted the structure-based design approach.

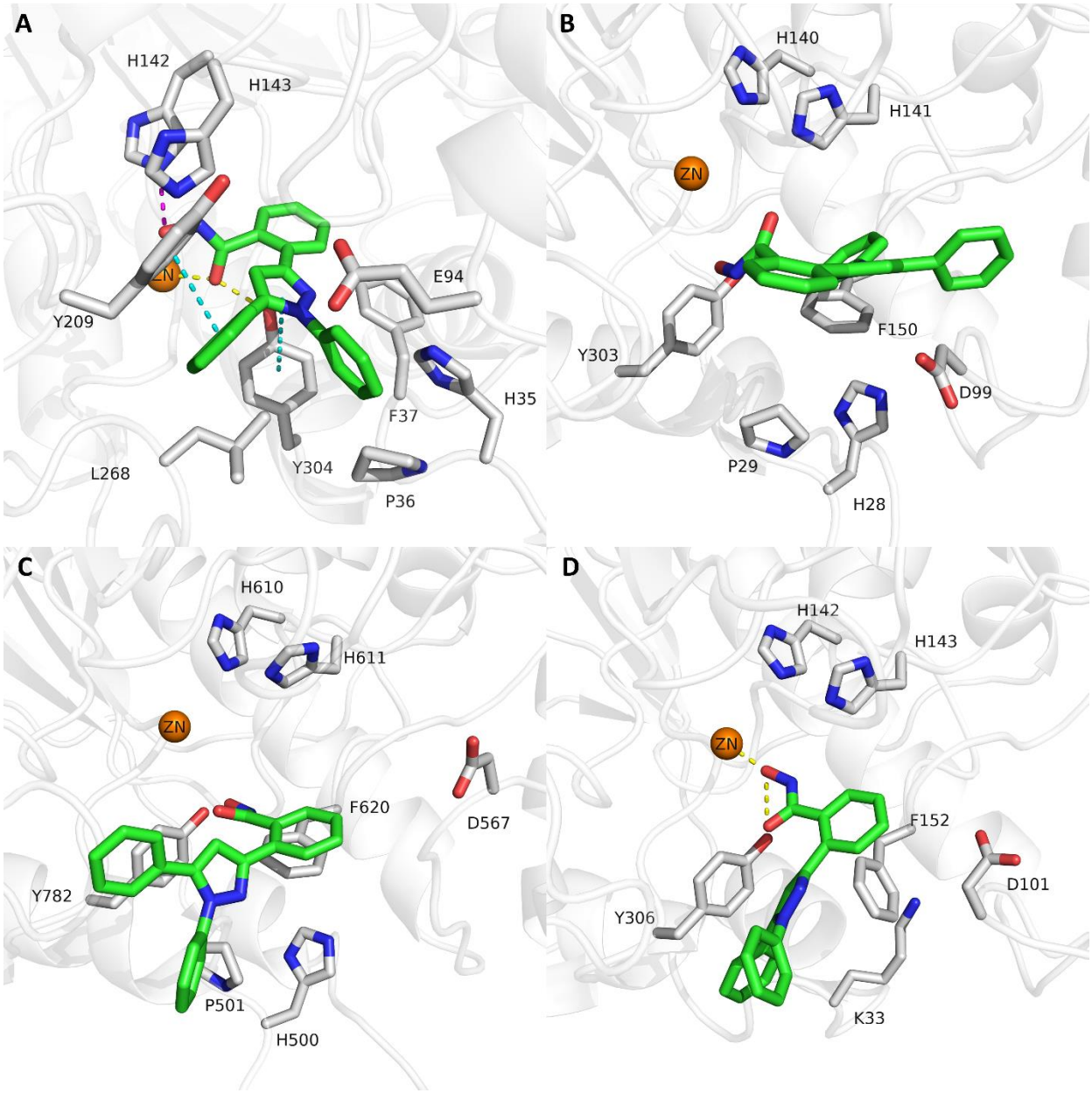

Figure. 5. Docked poses of **5a** (**A**) HDAC11. (**B**) HDAC1 (PDB 5ICN). (**C**) HDAC6 (PDB 5EDU). (**D**) HDAC8 (PDB 5FCW). The protein backbone appears as white cartoon, residues as grey sticks, zinc cofactor as orange sphere and compound **5a** as green sticks. Hydrogen bonds and coordination bonds are represented as yellow dashed lines, salt bridge as magenta dashed line and π-π interactions as cyan dashed lines.

3.5 Molecular Dynamics Simulations:

In order to validate the observed binding mode of **5a** in HDAC11 AlphaFold model, three independent short (50 ns) as well as single long (500 ns) molecular dynamics simulations were conducted. Analyzing the RMSD plots of the short runs showed that the protein-backbone atoms are stabilizing between 1 Å and 2 Å while the zinc ion is stabilizing at about 1 Å (**Figures 6A and 6B**). The ligand RMSD is similar

for the three runs and is stabilizing at about 2 Å all over the simulation time indicating a stable pose (**Figures 6C**). Inspecting the ligand RMSF plots confirmed the observed stability as all the ligand heavy atoms are fluctuating below 2 Å with the capping phenyl rings being the most fluctuating substructure (**Figures 6D**).

Interaction persistence showed very high stability for the salt bridge to His142 with persistence percent above 95% for the three independent runs, while the stability of the hydrogen bond to Tyr304 was also confirmed with persistence percent ranging between 76% and 88% (**Table S1**, **Figures S3** and **S4**).

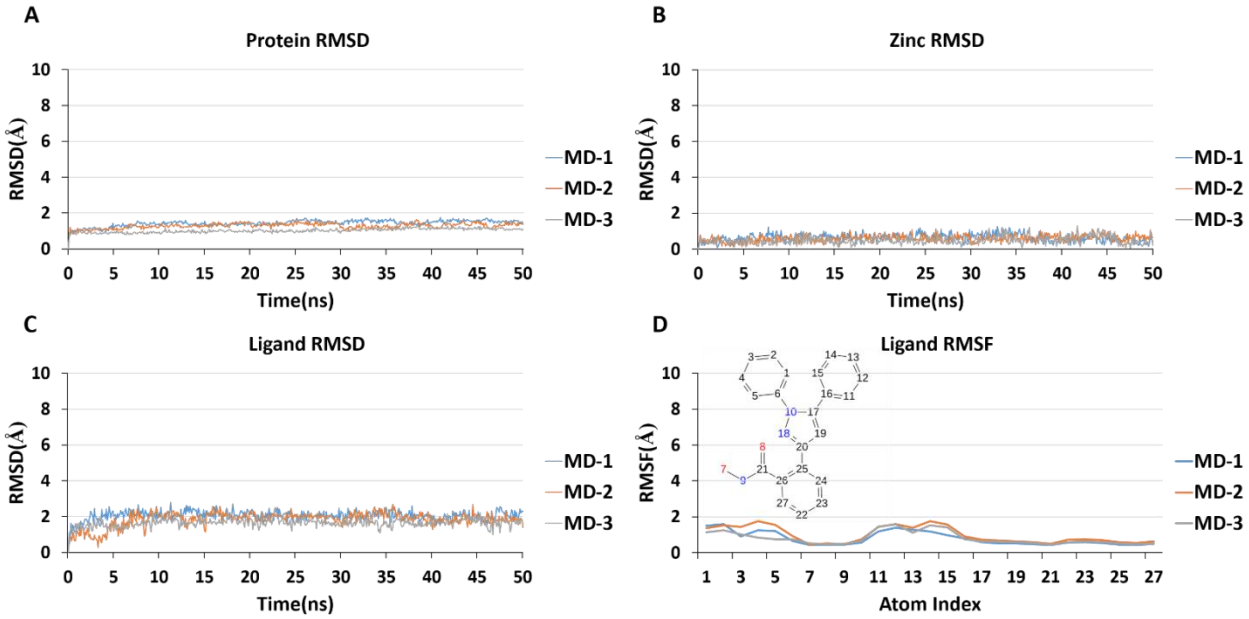

Figure 6. RMSD and RMSF plots of **5a** for three independent MD runs each for 50 ns. (**A**) RMSD plots of protein backbone heavy atoms. (**B**) RMSD plots of zinc ion. (**C**) RMSD plots of **5a** heavy atoms. (**D**) RMSF plots of **5a** heavy atoms.

The stability of the bidentate chelation mode observed initially in the docked pose was confirmed through monitoring the stability of the distance between the two chelator oxygen atoms of the zinc binding group and the zinc ion (**Figure 7**).

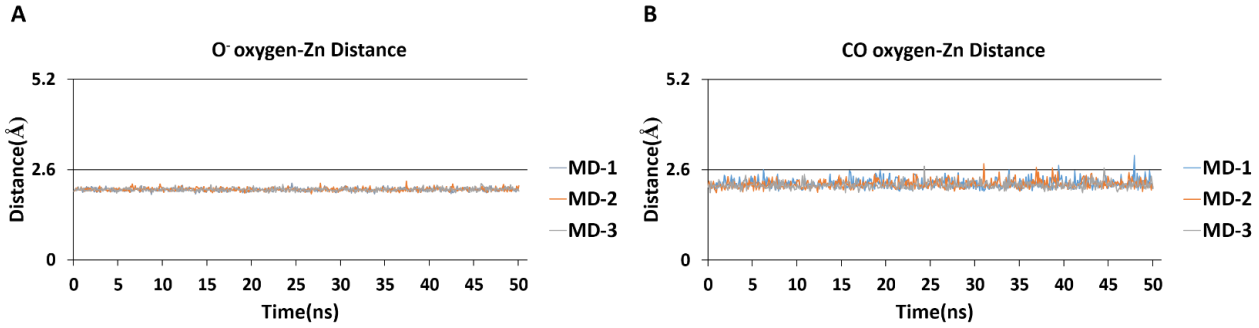

Figure 7. Distances to the zinc ion for three independent MD runs each for 50 ns. (**A**) and (**B)** are the hydroxyl and the carbonyl oxygen atoms of the zinc binding group respectively.

The RMSD plots of the protein and zinc ion obtained from the long molecular dynamics simulation are comparable to the short runs (**Figure 8A**) with the ligand RMSD stabilizing at 2 Å. The ligand RMSF plots showed that the most fluctuating substructures are the terminal phenyl capping groups (**Figures 8B, S5** and **S6**) while, the bidentate chelation was found to be stable all over the simulation (**Figures 8C** and **8D**).

In the long scale molecular dynamic simulation, the salt bridge stability to His142 was also confirmed with persistence percent of about 94%, however, the persistence percent for the hydrogen bond interaction with Tyr304 decreased to 38% (**Table S1**, **Figures S3** and **S4**). It is worth noting that such behavior of the hydrogen bond interaction with this conserved tyrosine residue was observed before in our previous study [16] and other studies [52] due to side chain flexibility [53, 54]. As a conclusion, the results from the molecular dynamics simulations proved the stability of the obtained ligand docking pose.

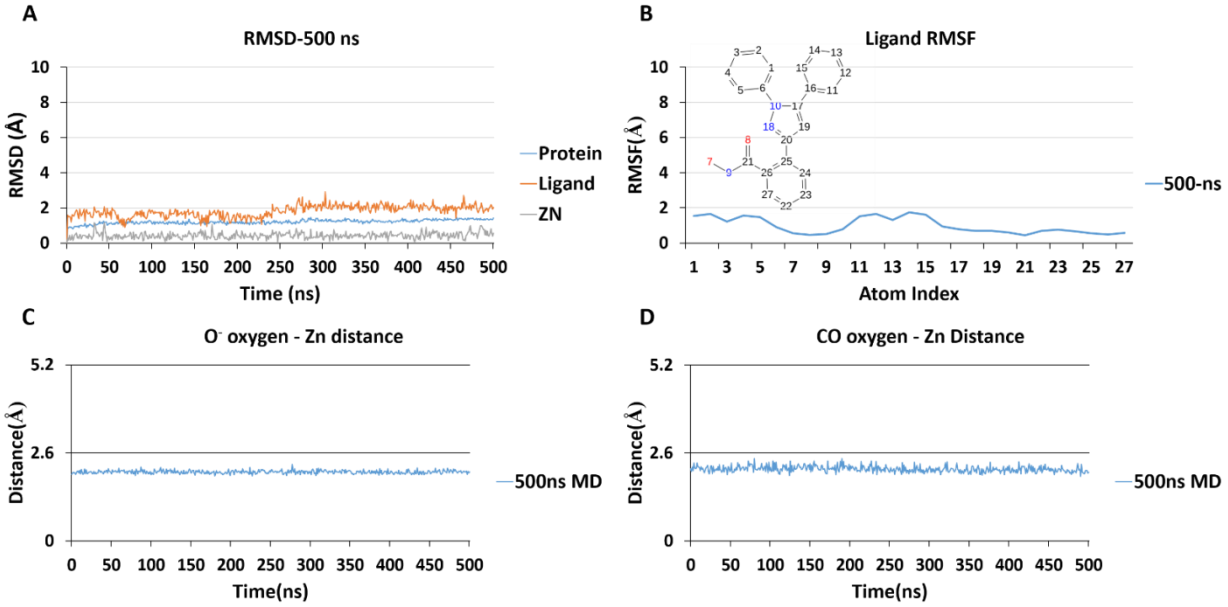

Figure. 8. (**A**) RMSD plots of the protein backbone heavy atoms, zinc ion and **5a** heavy atoms for the long MD run (500 ns). (**B**) RMSF plots of the **5a** heavy atom for the long MD run (500 ns). (**C**) and (**D**) are distances between the zinc ion and the hydroxyl and the carbonyl oxygen atoms of the zinc binding group, respectively, for the long MD runs (500 ns).

4 Conclusion:

To summarize, the previously optimized HDAC11 AlphaFold model was utilized for the structure-based design of new active and selective probes bearing a novel scaffold by using the docked pose of the

previously reported selective inhibitor FT895. Four compounds were synthesized and were first screened for inhibitory activity against different HDAC isoforms. Determining the IC_{50} for HDAC11 showed compound **5a** to be the most active and selective compound with a IC_{50} value of 365 nM for HDAC11 and no inhibition or weak inhibition for other HDAC subtypes at 10 µM concentration. Compound **5a** also possessed promising anti-neuroblastoma activity with EC_{50} of 3.6 µM. Docking of **5a** in the optimized HDAC11 AlphaFold model showed comparable binding mode to FT895 with the benzohydroxamic acid moiety of **5a** being inserted deeper in the binding pocket while one terminal phenyl ring is accommodated between the side chains of Tyr209 and Leu268 of loop 5 and loop 6 and the other terminal phenyl ring is directed towards loop 1 forming hydrophobic interactions thus fulfilling the aim of the initial design. The binding mode in terms of stability of the initially observed interactions and bidentate chelation was further validated using three independent short as well as single long molecular dynamic simulations.

Given the observed promising activity and selectivity of compound **5a**, additional chemical optimization is still to be considered to improve activity and selectivity. While compound **5a** interestingly demonstrated promising inhibition of cells viability of neuroblastoma cells, more investigations regarding the involvement of HDAC11 and the use of HDAC11 inhibitors in neuroblastoma cells are required.

In conclusion, utilization of the optimized HDAC11 AlphaFold model for structure-based design of new selective inhibitors with cellular activity was successful. The results of the current study show the possibility of using optimized AlphaFold models for the structure-based design of new lead structures and reflects the significance of the optimization procedure we previously adopted.

Supplementary Materials:

The following supporting information can be downloaded at XXX: Details on the carried out MD simulations.

Author Contributions:

F.B. did the computational studies, synthesized the compounds and wrote the manuscript. S. Hilscher carried out the HDAC in vitro testing. S.S. and S. Hagemann did the cellular testing. D.R. supervised the MD simulations. C.B. produced the HDAC4,5,7,9,10 and 11 for the enzymatic testing. S. Hüttelmaier supervised the cellular testing. M.S. supervised the in vitro testing and revised the manuscript. W.S. supervised the experiments and revised the manuscript.

Conflicts of Interest: The authors declare no conflict of interest

Funding: This study was supported by the Deutsche Forschungsgemeinschaft (DFG) grants 469954457 and 471614207 (W.S.). This work was in part supported by the CAS (RVO: 86652036) and the Grant Agency of the Czech Republic (24-12155S) (C.B.).

References:

1. Lombardi, P.M., K.E. Cole, D.P. Dowling, and D.W. Christianson, *Structure, mechanism, and inhibition of histone deacetylases and related metalloenzymes.* Curr Opin Struct Biol, 2011. **21**(6): p. 735-43.
2. Marek, M., T.B. Shaik, and C. Romier, *Structural Biology of Epigenetic Targets: Exploiting Complexity*, in *Epigenetic Drug Discovery*. 2019. p. 11-44.
3. Chen, H., C. Xie, Q. Chen, and S. Zhuang, *HDAC11, an emerging therapeutic target for metabolic disorders.* Front Endocrinol (Lausanne), 2022. **13**: p. 989305.
4. Liu, S.S., F. Wu, Y.M. Jin, W.Q. Chang, and T.M. Xu, *HDAC11: a rising star in epigenetics.* Biomed Pharmacother, 2020. **131**: p. 110607.
5. Deubzer, H.E., M.C. Schier, I. Oehme, M. Lodrini, B. Haendler, A. Sommer, and O. Witt, *HDAC11 is a novel drug target in carcinomas.* Int J Cancer, 2013. **132**(9): p. 2200-8.
6. Gong, D., Z. Zeng, F. Yi, and J. Wu, *Inhibition of histone deacetylase 11 promotes human liver cancer cell apoptosis.* Am J Transl Res, 2019. **11**(2): p. 983-990.
7. Huo, W., F. Qi, and K. Wang, *Long non-coding RNA BCYRN1 promotes prostate cancer progression via elevation of HDAC11.* Oncol Rep, 2020. **44**(3): p. 1233-1245.
8. Wang, W., L. Fu, S. Li, Z. Xu, and X. Li, *Histone deacetylase 11 suppresses p53 expression in pituitary tumor cells.* Cell Biol Int, 2017. **41**(12): p. 1290-1295.
9. Martin, M.W., J.Y. Lee, D.R. Lancia, Jr., P.Y. Ng, B. Han, J.R. Thomason, M.S. Lynes, C.G. Marshall, C. Conti, A. Collis, M.A. Morales, K. Doshi, A. Rudnitskaya, L. Yao, and X. Zheng, *Discovery of novel N-hydroxy-2-arylisoindoline-4-carboxamides as potent and selective inhibitors of HDAC11.* Bioorg Med Chem Lett, 2018. **28**(12): p. 2143-2147.
10. Bora-Singhal, N., D. Mohankumar, B. Saha, C.M. Colin, J.Y. Lee, M.W. Martin, X. Zheng, D. Coppola, and S. Chellappan, *Novel HDAC11 inhibitors suppress lung adenocarcinoma stem cell self-renewal and overcome drug resistance by suppressing Sox2.* Scientific Reports, 2020. **10**(1): p. 4722.

11. Bai, P., Y. Liu, L. Yang, W. Ding, P. Mondal, N. Sang, G. Liu, X. Lu, T.T. Ho, Y. Zhou, R. Wu, V.C. Birar, M.Q. Wilks, R.E. Tanzi, H. Lin, C. Zhang, W. Li, S. Shen, and C. Wang, *Development and Pharmacochemical Characterization Discover a Novel Brain-Permeable HDAC11-Selective Inhibitor with Therapeutic Potential by Regulating Neuroinflammation in Mice.* Journal of Medicinal Chemistry, 2023.

12. Kutil, Z., J. Mikešová, M. Zessin, M. Meleshin, Z. Nováková, G. Alquicer, A. Kozikowski, W. Sippl, C. Bařinka, and M. Schutkowski, *Continuous Activity Assay for HDAC11 Enabling Reevaluation of HDAC Inhibitors.* ACS Omega, 2019. **4**(22): p. 19895-19904.

13. Kutil, Z., Z. Novakova, M. Meleshin, J. Mikesova, M. Schutkowski, and C. Barinka, *Histone Deacetylase 11 Is a Fatty-Acid Deacylase.* ACS Chem Biol, 2018. **13**(3): p. 685-693.

14. Son, S.I., J. Cao, C.-L. Zhu, S.P. Miller, and H. Lin, *Activity-Guided Design of HDAC11-Specific Inhibitors.* ACS Chemical Biology, 2019. **14**(7): p. 1393-1397.

15. Ho, T.T., C. Peng, E. Seto, and H. Lin, *Trapoxin A Analogue as a Selective Nanomolar Inhibitor of HDAC11.* ACS Chemical Biology, 2023. **18**(4): p. 803-809.

16. Baselious, F., D. Robaa, and W. Sippl, *Utilization of AlphaFold models for drug discovery: Feasibility and challenges. Histone deacetylase 11 as a case study.* Comput Biol Med, 2023. **167**: p. 107700.

17. Gao, L., M.A. Cueto, F. Asselbergs, and P. Atadja, *Cloning and functional characterization of HDAC11, a novel member of the human histone deacetylase family.* J Biol Chem, 2002. **277**(28): p. 25748-55.

18. Jumper, J., R. Evans, A. Pritzel, T. Green, M. Figurnov, O. Ronneberger, K. Tunyasuvunakool, R. Bates, A. Žídek, A. Potapenko, A. Bridgland, C. Meyer, S.A.A. Kohl, A.J. Ballard, A. Cowie, B. Romera-Paredes, S. Nikolov, R. Jain, J. Adler, T. Back, S. Petersen, D. Reiman, E. Clancy, M. Zielinski, M. Steinegger, M. Pacholska, T. Berghammer, S. Bodenstein, D. Silver, O. Vinyals, A.W. Senior, K. Kavukcuoglu, P. Kohli, and D. Hassabis, *Highly accurate protein structure prediction with AlphaFold.* Nature, 2021. **596**(7873): p. 583-589.

19. David, A., S. Islam, E. Tankhilevich, and M.J.E. Sternberg, *The AlphaFold Database of Protein Structures: A Biologist's Guide.* J Mol Biol, 2022. **434**(2): p. 167336.

20. Ren, F., X. Ding, M. Zheng, M. Korzinkin, X. Cai, W. Zhu, A. Mantsyzov, A. Aliper, V. Aladinskiy, Z. Cao, S. Kong, X. Long, B.H. Man Liu, Y. Liu, V. Naumov, A. Shneyderman, I.V. Ozerov, J. Wang, F.W. Pun, D.A. Polykovskiy, C. Sun, M. Levitt, A. Aspuru-Guzik, and A. Zhavoronkov, *AlphaFold*

accelerates artificial intelligence powered drug discovery: efficient discovery of a novel CDK20 small molecule inhibitor. Chemical Science, 2023. **14**(6): p. 1443-1452.

21. Zhu, W., X. Liu, Q. Li, F. Gao, T. Liu, X. Chen, M. Zhang, A. Aliper, F. Ren, X. Ding, and A. Zhavoronkov, *Discovery of novel and selective SIK2 inhibitors by the application of AlphaFold structures and generative models.* Bioorganic & Medicinal Chemistry, 2023. **91**: p. 117414.
22. Díaz-Rovira, A.M., H. Martín, T. Beuming, L. Díaz, V. Guallar, and S.S. Ray, *Are Deep Learning Structural Models Sufficiently Accurate for Virtual Screening? Application of Docking Algorithms to AlphaFold2 Predicted Structures.* Journal of Chemical Information and Modeling, 2023. **63**(6): p. 1668-1674.
23. He, X.-h., C.-z. You, H.-l. Jiang, Y. Jiang, H.E. Xu, and X. Cheng, *AlphaFold2 versus experimental structures: evaluation on G protein-coupled receptors.* Acta Pharmacologica Sinica, 2023. **44**(1): p. 1-7.
24. Holcomb, M., Y.T. Chang, D.S. Goodsell, and S. Forli, *Evaluation of AlphaFold2 structures as docking targets.* Protein Sci, 2023. **32**(1): p. e4530.
25. Karelina, M., J.J. Noh, and R.O. Dror, *How accurately can one predict drug binding modes using AlphaFold models?* 2023, eLife Sciences Publications, Ltd.
26. Scardino, V., J.I. Di Filippo, and C.N. Cavasotto, *How good are AlphaFold models for docking-based virtual screening?* iScience, 2023. **26**(1): p. 105920.
27. *Schrödinger Release 2019-1: Maestro, Schrödinger, LLC, New York, NY, 2019.*
28. *Schrödinger Release 2019-1: Protein Preparation Wizard; Epik, Schrödinger, LLC, New York, NY, 2019; Impact, Schrödinger, LLC, New York, NY, 2019; Prime, Schrödinger, LLC, New York, NY, 2019.*
29. Sastry, G.M., M. Adzhigirey, T. Day, R. Annabhimoju, and W. Sherman, *Protein and ligand preparation: parameters, protocols, and influence on virtual screening enrichments.* J Comput Aided Mol Des, 2013. **27**(3): p. 221-34.
30. *Schrödinger Release 2019-1: Epik, Schrödinger, LLC, New York, NY, 2019*.
31. Greenwood, J.R., D. Calkins, A.P. Sullivan, and J.C. Shelley, *Towards the comprehensive, rapid, and accurate prediction of the favorable tautomeric states of drug-like molecules in aqueous solution.* J Comput Aided Mol Des, 2010. **24**(6-7): p. 591-604.
32. Shelley, J.C., A. Cholleti, L.L. Frye, J.R. Greenwood, M.R. Timlin, and M. Uchimaya, *Epik: a software program for pK(a) prediction and protonation state generation for drug-like molecules.* J Comput Aided Mol Des, 2007. **21**(12): p. 681-91.

33. Ghazy, E., T. Heimburg, J. Lancelot, P. Zeyen, K. Schmidtkunz, A. Truhn, S. Darwish, C.V. Simoben, T.B. Shaik, F. Erdmann, M. Schmidt, D. Robaa, C. Romier, M. Jung, R. Pierce, and W. Sippl, *Synthesis, structure-activity relationships, cocrystallization and cellular characterization of novel smHDAC8 inhibitors for the treatment of schistosomiasis.* European Journal of Medicinal Chemistry, 2021. **225**: p. 113745.

34. Ghazy, E., P. Zeyen, D. Herp, M. Hügle, K. Schmidtkunz, F. Erdmann, D. Robaa, M. Schmidt, E.R. Morales, C. Romier, S. Günther, M. Jung, and W. Sippl, *Design, synthesis, and biological evaluation of dual targeting inhibitors of histone deacetylase 6/8 and bromodomain BRPF1.* European Journal of Medicinal Chemistry, 2020. **200**: p. 112338.

35. Marek, M., T.B. Shaik, T. Heimburg, A. Chakrabarti, J. Lancelot, E. Ramos-Morales, C. Da Veiga, D. Kalinin, J. Melesina, D. Robaa, K. Schmidtkunz, T. Suzuki, R. Holl, E. Ennifar, R.J. Pierce, M. Jung, W. Sippl, and C. Romier, *Characterization of Histone Deacetylase 8 (HDAC8) Selective Inhibition Reveals Specific Active Site Structural and Functional Determinants.* Journal of Medicinal Chemistry, 2018. **61**(22): p. 10000-10016.

36. Vögerl, K., N. Ong, J. Senger, D. Herp, K. Schmidtkunz, M. Marek, M. Müller, K. Bartel, T.B. Shaik, N.J. Porter, D. Robaa, D.W. Christianson, C. Romier, W. Sippl, M. Jung, and F. Bracher, *Synthesis and Biological Investigation of Phenothiazine-Based Benzhydroxamic Acids as Selective Histone Deacetylase 6 Inhibitors.* Journal of Medicinal Chemistry, 2019. **62**(3): p. 1138-1166.

37. *Schrödinger Release 2019-1: LigPrep, Schrödinger, LLC, New York, NY, 2019.*

38. Harder, E., W. Damm, J. Maple, C. Wu, M. Reboul, J.Y. Xiang, L. Wang, D. Lupyan, M.K. Dahlgren, J.L. Knight, J.W. Kaus, D.S. Cerutti, G. Krilov, W.L. Jorgensen, R. Abel, and R.A. Friesner, *OPLS3: A Force Field Providing Broad Coverage of Drug-like Small Molecules and Proteins.* J Chem Theory Comput, 2016. **12**(1): p. 281-96.

39. Jorgensen, W.L., D.S. Maxwell, and J. Tirado-Rives, *Development and Testing of the OPLS All-Atom Force Field on Conformational Energetics and Properties of Organic Liquids.* Journal of the American Chemical Society, 1996. **118**(45): p. 11225-11236.

40. Jorgensen, W.L. and J. Tirado-Rives, *The OPLS [optimized potentials for liquid simulations] potential functions for proteins, energy minimizations for crystals of cyclic peptides and crambin.* Journal of the American Chemical Society, 1988. **110**(6): p. 1657-1666.

41. Shivakumar, D., J. Williams, Y. Wu, W. Damm, J. Shelley, and W. Sherman, *Prediction of Absolute Solvation Free Energies using Molecular Dynamics Free Energy Perturbation and the OPLS Force Field.* Journal of Chemical Theory and Computation, 2010. **6**(5): p. 1509-1519.

42. *Schrödinger Release 2019-1: Glide, Schrödinger, LLC, New York, NY, 2019.*

43. Friesner, R.A., J.L. Banks, R.B. Murphy, T.A. Halgren, J.J. Klicic, D.T. Mainz, M.P. Repasky, E.H. Knoll, M. Shelley, and J.K. Perry, *Glide: a new approach for rapid, accurate docking and scoring. 1. Method and assessment of docking accuracy.* Journal of medicinal chemistry, 2004. **47**(7): p. 1739-1749.

44. Friesner, R.A., R.B. Murphy, M.P. Repasky, L.L. Frye, J.R. Greenwood, T.A. Halgren, P.C. Sanschagrin, and D.T. Mainz, *Extra precision glide: Docking and scoring incorporating a model of hydrophobic enclosure for protein− ligand complexes.* Journal of medicinal chemistry, 2006. **49**(21): p. 6177-6196.

45. Halgren, T.A., R.B. Murphy, R.A. Friesner, H.S. Beard, L.L. Frye, W.T. Pollard, and J.L. Banks, *Glide: a new approach for rapid, accurate docking and scoring. 2. Enrichment factors in database screening.* Journal of medicinal chemistry, 2004. **47**(7): p. 1750-1759.

46. *Schrödinger Release 2019-1; Desmond Molecular Dynamics System, D.E. Shaw Research: New York, NY, USA, 2019; Maestro-Desmond Interoperability Tools, Schrödinger: New York, NY, USA, 2019*.

47. Bowers, K.J., D.E. Chow, H. Xu, R.O. Dror, M.P. Eastwood, B.A. Gregersen, J.L. Klepeis, I. Kolossvary, M.A. Moraes, F.D. Sacerdoti, J.K. Salmon, Y. Shan, and D.E. Shaw. *Scalable Algorithms for Molecular Dynamics Simulations on Commodity Clusters*. in *SC '06: Proceedings of the 2006 ACM/IEEE Conference on Supercomputing*. 2006.

48. Zessin, M., Z. Kutil, M. Meleshin, Z. Nováková, E. Ghazy, D. Kalbas, M. Marek, C. Romier, W. Sippl, C. Bařinka, and M. Schutkowski, *One-Atom Substitution Enables Direct and Continuous Monitoring of Histone Deacylase Activity.* Biochemistry, 2019. **58**(48): p. 4777-4789.

49. Heimburg, T., F.R. Kolbinger, P. Zeyen, E. Ghazy, D. Herp, K. Schmidtkunz, J. Melesina, T.B. Shaik, F. Erdmann, M. Schmidt, C. Romier, D. Robaa, O. Witt, I. Oehme, M. Jung, and W. Sippl, *Structure-Based Design and Biological Characterization of Selective Histone Deacetylase 8 (HDAC8) Inhibitors with Anti-Neuroblastoma Activity.* Journal of Medicinal Chemistry, 2017. **60**(24): p. 10188-10204.

50. Ismail, N.S.M., R.F. George, R.A.T. Serya, F.N. Baselious, M. El-Manawaty, E.M. Shalaby, and A.S. Girgis, *Rational design, synthesis and 2D-QSAR studies of antiproliferative tropane-based compounds.* RSC Advances, 2016. **6**(104): p. 101911-101923.

51. Thole, T.M., M. Lodrini, J. Fabian, J. Wuenschel, S. Pfeil, T. Hielscher, A. Kopp-Schneider, U. Heinicke, S. Fulda, O. Witt, A. Eggert, M. Fischer, and H.E. Deubzer, *Neuroblastoma cells depend on HDAC11 for mitotic cell cycle progression and survival.* Cell Death Dis, 2017. **8**(3): p. e2635.

52. Bülbül, E.F., J. Melesina, H.S. Ibrahim, M. Abdelsalam, A. Vecchio, D. Robaa, M. Zessin, M. Schutkowski, and W. Sippl, *Docking, Binding Free Energy Calculations and In Vitro Characterization of Pyrazine Linked 2-Aminobenzamides as Novel Class I Histone Deacetylase (HDAC) Inhibitors.* Molecules, 2022. **27**(8): p. 2526.

53. Liu, J., Y. Yu, J. Kelly, D. Sha, A.-B. Alhassan, W. Yu, M.M. Maletic, J.L. Duffy, D.J. Klein, M.K. Holloway, S. Carroll, B.J. Howell, R.J.O. Barnard, S. Wolkenberg, and J.A. Kozlowski, *Discovery of Highly Selective and Potent HDAC3 Inhibitors Based on a 2-Substituted Benzamide Zinc Binding Group.* ACS Medicinal Chemistry Letters, 2020. **11**(12): p. 2476-2483.

54. Whitehead, L., M.R. Dobler, B. Radetich, Y. Zhu, P.W. Atadja, T. Claiborne, J.E. Grob, A. McRiner, M.R. Pancost, A. Patnaik, W. Shao, M. Shultz, R. Tichkule, R.A. Tommasi, B. Vash, P. Wang, and T. Stams, *Human HDAC isoform selectivity achieved via exploitation of the acetate release channel with structurally unique small molecule inhibitors.* Bioorganic & Medicinal Chemistry, 2011. **19**(15): p. 4626-4634.